Internal gravity waves in the thermosphere during low and high solar activity: Simulation study

Erdal Yiğit[1,2] and Alexander S. Medvedev[3]

Received 17 November 2009; revised 15 March 2010; accepted 6 April 2010; published 4 August 2010.

[1] Propagation of internal gravity waves (GWs) from the lower atmosphere into the upper thermosphere, and their dynamical and thermal effects have been studied under low and high solar activity approximated by the $F_{10.7}$ parameter. It has been done by using a nonlinear spectral parameterization in systematic offline calculations with typical wind and temperature distributions from the HWM and MSISE-90 models, and with interactive simulations using the University College London Coupled Middle Atmosphere-Thermosphere-2 (CMAT2) general circulation model (GCM) under solstice conditions. The estimates have been performed for relatively slow harmonics with horizontal phase velocities less than 100 m s^{-1}, which are not affected by reflection and/or ducting. GW drag and wave-induced heating/cooling are shown to be smaller below ~170 km at high solar activity, and larger above. The maxima of GW momentum deposition occur much higher in the upper thermosphere, but their peaks are half as strong, 120 vs 240 m s^{-1} day^{-1} in the winter hemisphere when the insolation is large. Instead of strong net cooling in the upper thermosphere, GWs produce a weak heating at high solar activity created by fast harmonics less affected by dissipation. Molecular viscosity increases with solar activity at fixed pressure levels, but seen in Cartesian altitude grids it can either increase or decrease in the lower thermosphere, depending on the height. Therefore, in pressure coordinates, in which most GCMs operate, the influence of larger temperatures can be viewed as a competition between the enhanced dissipation and vertical expansion of the atmosphere.

Citation: Yiğit, E., and A. S. Medvedev (2010), Internal gravity waves in the thermosphere during low and high solar activity: Simulation study, *J. Geophys. Res.*, *115*, A00G02, doi:10.1029/2009JA015106.

1. Introduction

[2] Gravity waves (GWs) generated in the lower atmosphere represent an important source of energy and momentum in the mesosphere and lower thermosphere (MLT). Higher in the thermosphere and ionosphere (TI), GWs are almost continuously present. They often manifest themselves as traveling ionospheric disturbances (TIDs), which are excited by auroral sources at high-latitudes, have fast horizontal velocities and large horizontal scales, and can propagate thousands of kilometers equatorward [*Francis*, 1975; *Richmond*, 1978]. Meanwhile, there is growing observational evidence that GWs of tropospheric origin are capable of penetrating into and perturbing the upper thermosphere significantly [*Oliver et al.*, 1997; *Djuth et al.*, 2004; *Livneh et al.*, 2007; *Klausner et al.*, 2009]. Some observational studies have related GW signatures in the TI to meteorological events in the lower atmosphere [*Hocke and Tsuda*, 2001; *Bishop et al.*, 2006]. Thermospheric variability associated with the geomagnetic and solar activities alter the propagation of internal GWs. As a result, a strong relationship between the GW activity in the F_2 layer and the geomagnetic and solar conditions has been found [*Klausner et al.*, 2009]. This paper addresses the issue of how variations of the solar radiation flux, approximated by the variation of the $F_{10.7}$ parameter, affect GWs propagating from the lower atmosphere to the upper thermosphere, and what response these waves produce in the thermosphere above the turbopause.

[3] Unlike in the middle atmosphere, propagation of GWs in the TI is strongly influenced by dissipation. The latter is mainly due to molecular viscosity and heat conduction, but "ion friction" caused by the interaction of the ionized atmosphere with the neutral flow is also a significant source of wave dissipation. Changes in the solar radiation absorption do not affect the dynamics of wave propagation directly. Instead, they modify the thermospheric temperature and winds, and thus, alter the density, static stability, dissipation, and refractive properties associated with the Doppler shift by the mean wind. Propagation of GWs in the dissipative thermosphere as well as their possible effects in the TI have been

[1]Center for Space Environment Modeling, Department of Atmosphere, Oceanic and Space Sciences, University of Michigan, Ann Arbor, Michigan, USA.
[2]Atmospheric Physics Laboratory, Department of Physics and Astronomy, University College London, London, UK.
[3]Max Planck Institute for Solar System Research, Katlenburg-Lindau, Germany.

0148-0227/10/2009JA015106

studied theoretically and numerically. However, insights into the links between the changes in the thermosphere driven by the solar radiation and GW responses remain very limited.

[4] Characteristics of GW propagation in hot versus cold thermospheres was studied to some extent in the work by *Hickey* [1986, 1987]. *Vadas and Fritts* [2006], *Vadas* [2007], and *Fritts and Vadas* [2008] used a ray tracing model based on the full viscous dispersion relation [*Vadas and Fritts*, 2005] to calculate the propagation of individual harmonics and a coherent spectrum of GWs excited in the troposphere by deep convective sources. In their sensitivity study at high solar activity with several model profiles of temperature and molecular viscosity, they found: (1) reduced atmospheric stability and dissipation enhance wave propagation; (2) reflection increases for harmonics with shorter horizontal scales, and competes with the enhanced propagation. These findings are in good agreement with conclusions of earlier studies [*Francis*, 1973; *Richmond*, 1978; *Cole and Hickey*, 1981], and are applicable to increased thermospheric temperatures during active solar and/or daytime conditions.

[5] In this paper, we make a step further from sensitivity estimates for individual harmonics to assessing gross effects of low and high solar activity on GW spectra, and of the dynamical and thermal response of the mean circulation in the TI produced by the vertically propagating waves. This is done within the framework of fully interactive simulations with the Coupled Middle Atmosphere-Thermosphere-2 (CMAT2) model employing our recently developed spectral nonlinear GW scheme suitable for thermosphere general circulation models (GCMs) [*Yiğit et al.*, 2008]. This parameterization tracks the vertical propagation of multiple GW harmonics from their source regions in the lower atmosphere to the top of the model domain in the upper thermosphere. It accounts for the refraction of waves by the mean wind and temperature, nonlinear self-interactions, dissipation due to molecular and eddy viscosity and thermal conduction, ion friction, and breaking. It has been shown that accounting for wave dissipation properly in a GW parameterization generates a considerable body forcing in the simulated TI. In particular, dynamical effects of GWs emanating from the troposphere are not only non-negligible above the turbopause, but are comparable to those of ion drag up to at least 180–200 km [*Yiğit et al.*, 2009]. Thermal effects of dissipating GWs result mainly in an effective cooling (up to 100 to 180 K day^{-1} around 200 km) associated with the convergence of the induced downward heat fluxes [*Yiğit and Medvedev*, 2009]. Accounting for GWs in the CMAT2 GCM has helped to bring simulated wind and temperature fields in the TI closer to the Horizontal Wind Model (HWM) and MSISE-90 empirical models. This study follows the general framework of our recent simulations, but focuses on the consequences of low and high insolation for GW propagation and dissipation in the thermosphere.

[6] The structure of this paper is as follows: The spectral nonlinear GW scheme is outlined briefly in section 2. Typical variations of the background atmospheric parameters as functions of the solar activity are discussed in section 3. Results of the offline calculations for several profiles from HWM and MSISE-90 empirical models at low and high solar activity conditions are described in sections 4 and 5 for the atmosphere without and with wind shear, respectively. A short description of the CMAT2 GCM is given in section 6. Results of GCM simulations are presented in section 7. Finally, a brief summary and conclusions are given in section 8.

2. Gravity Wave Scheme

[7] Gravity wave parameterizations calculate average effects of unresolved (subgrid-scale) waves on the resolved (mean) fields in GCMs. Wave propagation is described in terms the vertical flux of the horizontal momentum associated with a harmonic j, ρF_j, where $F_j = \overline{u'w'}_j$ is the momentum flux per unit mass, ρ is the density, u' and w' are the horizontal and vertical components of wind perturbations, and the overline denotes an appropriate averaging over subgrid scales. F_j varies with height according to [*Yiğit et al.*, 2008]

$$F_j(z) = F_j(z_0)\rho(z_0)\rho^{-1}(z)\tau_j(z). \quad (1)$$

In the above equation, z_0 is the reference (or source) level, and τ_j is the transmissivity function. For conservative propagation $\tau_j = 1$, no divergence of the flux ρF_j takes place, and no average effect is produced by the harmonic on the mean flow. In case of dissipative propagation, τ_j can be represented as

$$\tau_j(z) = \exp\left\{-\int_{z_0}^{z}\left[\beta^j_{mol} + \beta^j_{ion} + \beta^j_{eddy} + \beta^j_{newt} + \beta^j_{non}\right]dz'\right\}, \quad (2)$$

where the flux attenuation functions β^j are attributed to different dissipation mechanisms. Vertical damping rates due to molecular viscosity and thermal conduction (assuming that the Prandtl number is equal to unity) β^j_{mol}, and due to ion friction β^j_{ion} have forms [*Yiğit et al.*, 2008, and references therein]

$$\beta^j_{mol} = \frac{2\nu_{mol}N^3}{k_h|c_j - \overline{u}|^4}, \quad (3)$$

$$\beta^j_{ion} = \frac{2\nu_{ni}N}{k_h|c_j - \overline{u}|^2}, \quad (4)$$

where N is the buoyancy frequency; k_h and c_j are the horizontal wavelength and phase speed of the harmonic j, respectively; $\overline{u}(z)$ is the mean horizontal wind; ν_{mol} is the kinematic molecular viscosity; ν_{ni} is the neutral-ion collision frequency. Dissipation due to the background atmospheric eddy viscosity, β_{eddy}, is described by the equation similar to (3) with ν_{mol} replaced with the eddy diffusion coefficient, D_{eddy}, and the expression for the radiative damping in the form of the Newtonian cooling, β_{newt} is analogous to that for the ion friction (4) with the Newtonian cooling coefficient α_{newt}, instead of ν_{ni}. β_{non} describes the dissipation of the harmonic j caused by nonlinear interactions with other waves in the spectrum. This dissipation is the result of instabilities on scales shorter than the vertical wavelength of the harmonic. If the spectrum consists of a single harmonic, the wave interacts nonlinearly with itself referred to as "self-interaction", and the corresponding β_{non} describes the well-known Hodges-Lindzen breaking due to convective

instability. For a spectrum with multiple waves, β_{non} takes the form [*Medvedev and Klaassen*, 1995, 2000]

$$\beta_{non} = \frac{\sqrt{2\pi}N}{\sigma_j}\exp\left(-\frac{|c_j-\overline{u}|^2}{2\sigma_j^2}\right), \quad (5)$$

where the variance σ_j^2 is created by velocity fluctuations due to harmonics with shorter vertical scales, i.e., $\sigma_j^2 = \Sigma_{m_i>m_j} u_i'^2$, m being the vertical wave number.

[8] Once the wave flux F is specified at the source level z_0, equation (1) can be integrated upwards for all harmonics. The acceleration/deceleration ("GW drag") imposed by dissipating GWs on the mean wind is given by the divergence of the wave momentum flux divided by the mean density taken with the opposite sign:

$$a = \sum_j a_j \equiv -\sum_j \rho^{-1}(\rho F_j)_z, \quad (6)$$

where a_j is the contribution of an individual harmonic. Heating and cooling produced by GWs can be calculated from [*Medvedev and Klaassen*, 2003; *Yiğit and Medvedev*, 2009]

$$\epsilon_{GW} = \sum_j \left\{ \underbrace{\frac{(c_j-\overline{u})a_j}{c_p}}_{E_j} + \underbrace{\frac{H}{2\rho R}\frac{\partial}{\partial z}[\rho(c_j-\overline{u})a_j]}_{Q_j} \right\}. \quad (7)$$

In (7), c_p is the specific heat at constant pressure, H is the density scale height, R is the universal gas constant. The first term in the brackets on the right-hand side of (7) represents the irreversible heating due to the mechanical energy conversion, E_j, and the second one is the convergence of the induced heat flux, Q_j. As with many GW parameterizations, our scheme assumes vertically propagating harmonics under steady wave approximation. This effectively implies that subgrid-scale waves do not leave grid columns while propagating to the top of the model. For that, we limit our consideration by relatively slow GWs with horizontal phase speeds less than 100 m s^{-1}. Harmonics with $c < 60$ m s^{-1} are important in the MLT, while faster waves with $60 < c < 80$ to 100 m s^{-1} provide significant forcing in the TI [*Vadas and Liu*, 2009; *Yiğit et al.*, 2009]. Typical horizontal wavelengths, λ_h, of GWs observed in the thermosphere are usually in the range of ~100 to 500 km. Waves with $\lambda_h \sim 100$ to 300 km often produce best results (that is, agreement between simulations and observations) when GW schemes are used in middle atmosphere GCMs. Therefore, we employ $k_h = 2\pi/300$ km throughout the calculations to be presented here. This setup excludes many of high-frequency and short-scale harmonics generated by convective sources. Such larger-scale GWs escape reflection in the TI associated with the decreasing stability (lower N) [*Fritts and Vadas*, 2008].

3. Background Atmospheric Properties at High and Low Solar Activities

[9] It is seen from (3)–(5) that the modulation of the mean atmospheric state induced by variable solar radiation absorption enter the GW scheme via N, temperature dependence of $\nu_{mol}(T)$, and of other dissipation coefficients. Changes in the temperature alter the mean wind $\overline{u}$, and thus, affect the dispersion relation and the vertical damping rate β, as well. Following from (6) and (7), the changes in the density profiles, $\rho(z)$, modify the dynamical and thermal feedback of GWs on the mean flow.

[10] Typical temperature profiles from MSISE-90 model for June $F_{10.7} = 80 \times 10^{-22}$ W m^{-2} Hz^{-1} and $F_{10.7} = 180 \times 10^{-22}$ W m^{-2} Hz^{-1} are plotted for 60°N in Figure 1a. Hereafter, we shall refer to these values of $F_{10.7}$ as low and high solar activities, respectively. The neutral temperature below 120 km is practically not affected by the solar flux variations. Above, the temperature at high solar activity, T^{high}, reaches 1400 K in the exosphere exceeding the one during the low activity, T^{low}, by more than 550 K, and by about 500 K at the F_2 layer heights. Note that the upward expansion of the thermosphere at higher temperatures leads to higher pressures at fixed altitudes. From the ideal gas equation, $\rho = p/RT$, the density is the ratio of both increasing pressure p and T, and, generally, can either rise or drop when the solar activity grows depending on a particular p and T. As a result, the molecular kinematic viscosity calculated after *Banks and Kockarts* [1973],

$$\nu_{mol} = 3.563 \times 10^{-7} T^{0.69}/\rho \quad [\mathrm{m^2\ s^{-1}}], \quad (8)$$

is determined by the particular vertical profiles of $\rho(z)$ and $T(z)$, and can grow less or more rapidly with height during high solar activity in the TI. Figure 1b demonstrates that $\nu_{mol}^{high}(z) < \nu_{mol}^{low}(z)$ above ≈175 km, and the opposite takes place between ≈125 and 175 km. The neutral-ion collision frequency, ν_{ni}, shows some variations with height with slightly larger ν_{ni}^{high} in the upper thermosphere (Figure 1c). The buoyancy frequency (Figure 1d) monotonically decreases above 150 km when the temperature rises. The neutral gas density falls exponentially with height having larger values at high solar activity (Figure 1e). The zonal wind demonstrates a reversal in the MLT and fast thermospheric speeds (Figure 1f). Upper thermospheric easterlies at high solar activity are slower than those at low activity.

[11] Most GCMs employ pressure levels as vertical coordinates rather than a geometrical height. Therefore, we plotted the relative variations of background parameters at 60°S, 0° and 60°N, $(X^{high} - X^{low})/X^{low}$, as functions of pressure. It is immediately seen from Figure 2 that the relative changes have very weak latitudinal dependence, except for ν_{ni}. The latter is the function of the ion density n_i [*Klostermeyer*, 1972],

$$\nu_{ni} = 7.22 \times 10^{-17} T^{0.37} n_i, \quad (9)$$

and, thus, is controlled by the Earth's magnetic field displaced with respect to the geographical poles. Under the assumption of charge neutrality, the ion densities are evaluated using electron density data from the CHIU ionosphere model [*Chiu*, 1975]. The temperature rises by ≈40% when the solar flux is high (Figure 2a), and the density, $\rho = p/RT$, falls almost proportionally on the fixed pressure levels. The molecular viscosity (Figure 2b) increases monotonically by up to 100% near the model top. From (8), $\nu_{mol} \sim T^{1+0.69}$ when the pressure is fixed, and $\nu_{mol}(p)$ rises when temperature grows. Note that the latter case is opposite to what occurs in the Cartesian vertical coordinates in the upper thermosphere

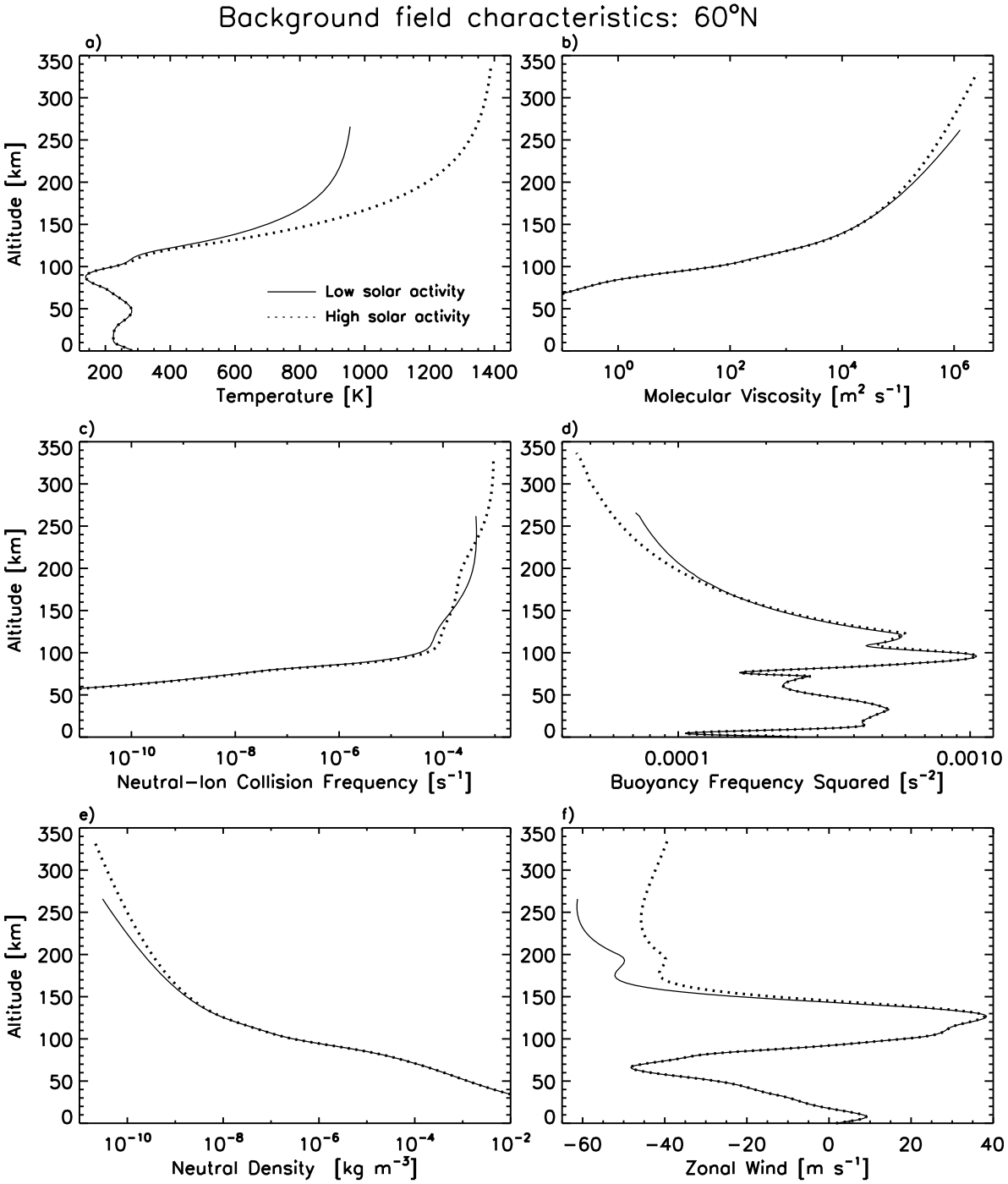

Figure 1. Vertical profiles of (a) background temperature from MSISE-90, (b) molecular viscosity, (c) neutral-ion collision frequency, (d) Brunt-Väisälä frequency squared, (e) neutral density, and (f) zonal wind from HWM on 22 June at 60°N as functions of geometrical altitude. Solid and dotted lines are for low and high solar activities, respectively.

(Figure 1b). Both results can be reconciled if one recalls that the same pressure level corresponds to higher geometrical altitude when the temperatures are higher. The values of neutral-ion collision frequency (Figure 2c) are generally larger (up to 140% in the upper thermosphere), depend on the latitude, and somewhat decrease near the F_2 layer heights in the winter hemisphere during stronger solar activity. The buoyancy frequency gradually decreases with height by about 40% in the exosphere (Figure 2d).

4. Column Model Calculations in the Windless Atmosphere

[12] Having outlined typical changes of temperature, atmospheric stability and dissipation during low and high solar

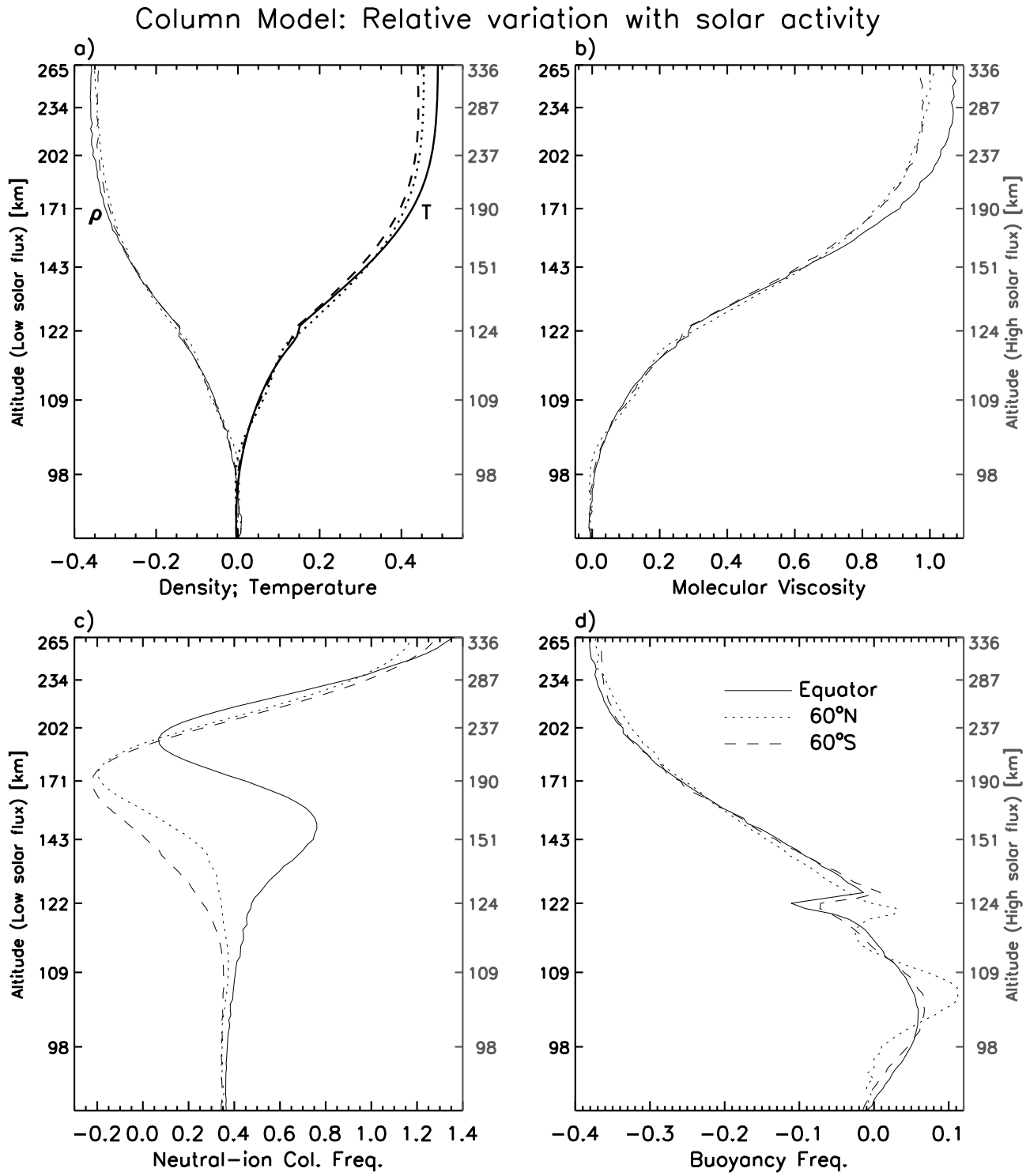

Figure 2. Relative variations of (a) neutral density (thin) and temperature (thick), (b) molecular viscosity, (c) neutral-ion collision frequency, and (d) buoyancy frequency with solar activity at three representative latitudes: 0° (solid), 60°S (dashed), and 60°N (dotted). Geometrical heights for solar minimum and maximum are shown on the left and right, respectively.

activity, we now investigate their net influences on GWs. In this section, we analyze the vertical propagation of multiple harmonic spectra with off-line calculations for representative background profiles described in section 3. An appropriate distribution of GW momentum fluxes, F_j, must be specified at a source level, z_0, in the lower atmosphere as a function of horizontal phase speeds, c_j, where positive and negative c_j correspond to eastward and westward propagating harmonics,

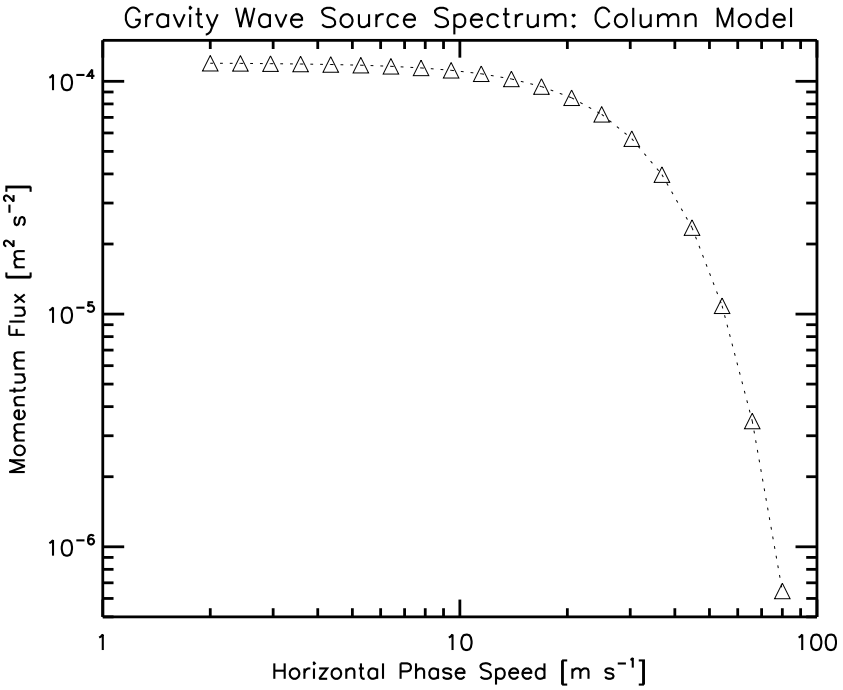

Figure 3. GW source spectrum used in calculations for the windless atmosphere (equation (10)). Both axes are logarithmically scaled. The magnitude of momentum flux for each wave harmonic is shown with small triangles. Spectral parameters are $c_w = 35$ m s^{-1}, $\overline{u'w'}_{\max} = 0.00014$ m^2 s^{-2}, M/2 = 20, and $c_{\max} = 80$ m s^{-1}.

respectively. The mathematical representation of such spectrum is given by *Yiğit et al.* [2008]:

$$\overline{u'w_j'}(z_0) = \mathrm{sgn}(c_j - \overline{u}_0)\overline{u'w'}_{\max} \exp[-(c_j - c_s)^2/c_w^2], \qquad (10)$$

where $\overline{u'w'}_{\max}$ is the maximum momentum flux; $\overline{u}_0 = \overline{u}(z_0)$ is the mean wind at the source level; c_s is the spectral shift; and c_w is the half-width of the Gaussian distribution. In this paper, we will be using a symmetric spectrum, i.e., c_s and $\overline{u}_0$ are zero. Thus, eastward/westward propagating harmonics with the same $|c|$ carry equal amounts of eastward/westward momentum.

[13] In the simplest possible case, the reflection and critical level filtering are eliminated by assuming a windless atmosphere, i.e., $\overline{u} = 0$. With this setup, non-zero GW drag can be produced if the spectrum is not symmetric with respect to $c = 0$, that is, if the momentum deposition by individual harmonics is not exactly canceled by that of counterpart waves traveling in the opposite direction. Thus, we employ the same spectrum as presented in the work by *Yiğit and Medvedev* [2009], but consider only eastward propagating harmonics, $c_j > 0$, as used in the work by *Yiğit et al.* [2008, section 6]. We assume 20 GW harmonics distributed logarithmically in the phase speed spectrum [*Medvedev and Klaassen*, 2000] with phase velocities from 2 to 80 m s^{-1}, i.e., $c_{\max} = 80$ m s^{-1}, $\overline{u'w'}_{\max} = 0.00014$ m^2 s^{-2}, and $c_w = 35$ m s^{-1} as shown in Figure 3.

[14] The combined effect of static stability, density, and dissipation at two MSISE-90 temperature profiles corresponding to the low and high $F_{10.7}$ is illustrated in Figure 4. The vertical damping rates associated with molecular diffusion and thermal conduction, β_{mol}; ion friction, β_{ion}; and nonlinear interactions between the waves, β_{non}, are shown for two harmonics with phase velocities $c = 80$ m s^{-1} and $c = 54$ m s^{-1}. Figure 4 is plotted in log-pressure coordinates, but the geometrical height is given on the left and right hand sides for low and high solar activities, respectively. It is seen that, in the absence of the mean wind, the phase velocity represents a scaling factor for β_{mol} and β_{ion} with faster waves experiencing weaker damping. For β_{non}, the behavior is more complex as the dissipation depends not on the phase velocity itself, but on the amplitudes and phase velocities of other harmonics in the spectrum. Below 110–120 km, dissipation due to ion friction, although small, exceeds the dissipation by molecular diffusion. Above, β_{mol} dominates β_{ion}. In the MLT, where amplitudes of GWs are large, the nonlinear diffusion is the major damping mechanism. Inspection of Figure 4a shows that β_{mol} is always stronger (by tens of percent) during high solar activity when viewed in pressure coordinates. This result agrees well with that of *Hickey* [1986]. In Cartesian altitude coordinates, it actually becomes weaker above ~180 km when the thermosphere becomes hotter. The temperature dependence of β_{ion} is more complex, but, generally, the latter is stronger below 150–170 km, and weaker above at high solar activity. The total effect of β_{mol}, β_{ion}, and β_{non} on the momentum flux associated with GW harmonics is shown in Figure 4d: waves tend to dissipate lower (i.e., at higher pressures) when the thermospheric temperature increases. Note that faster harmonics, which are less attenuated by the enhanced dissipation below ~180 km, can probably penetrate above this height. There, they are subject to weaker dissipation when $F_{10.7}$ is higher, and thus, experience more favorable propagation conditions, as was

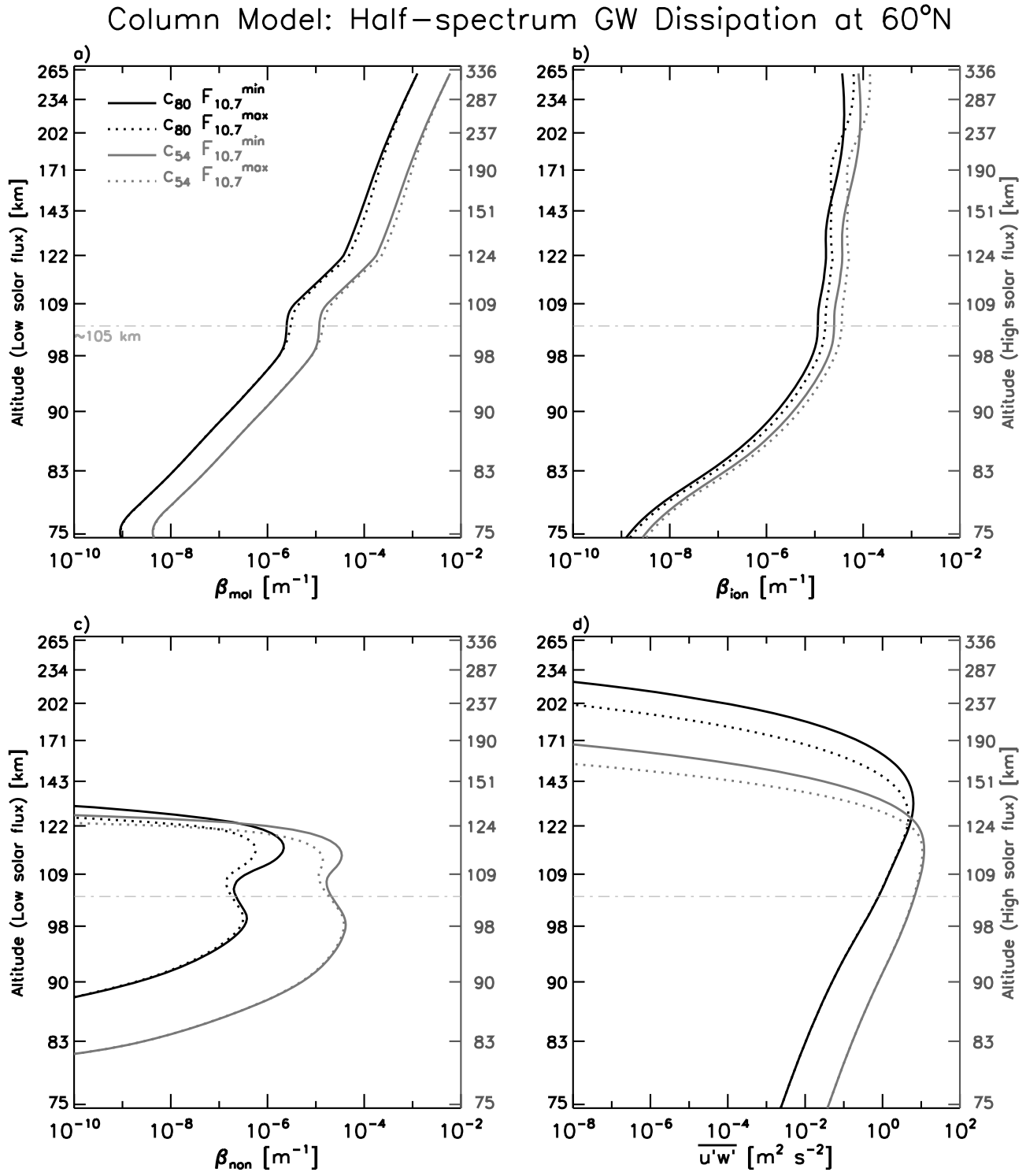

Figure 4. GW vertical damping rates calculated at 60°N for harmonics c = 54 (grey) and 80 m s^{-1} (black) due to (a) molecular viscosity, (b) ion friction, and (c) nonlinear diffusion. (d) The GW horizontal momentum fluxes are shown. Solid and dotted lines are for the solar minimum and maximum, respectively. The results are plotted on fixed pressure levels, but the corresponding geometrical heights are shown on the left and right vertical axis for low and high solar activity.

discussed in the works of *Vadas and Fritts* [2006] and *Fritts and Vadas* [2008].

[15] GW drag and wave-induced heating/cooling of the mean flow produced by the entire spectrum reflect the changes in the vertical propagation discussed above. Since the main wave damping for the given spectrum occurs below 180 km, GW drag is about 50 m s^{-1} day^{-1} weaker when the dissipation is enhanced during high solar activity

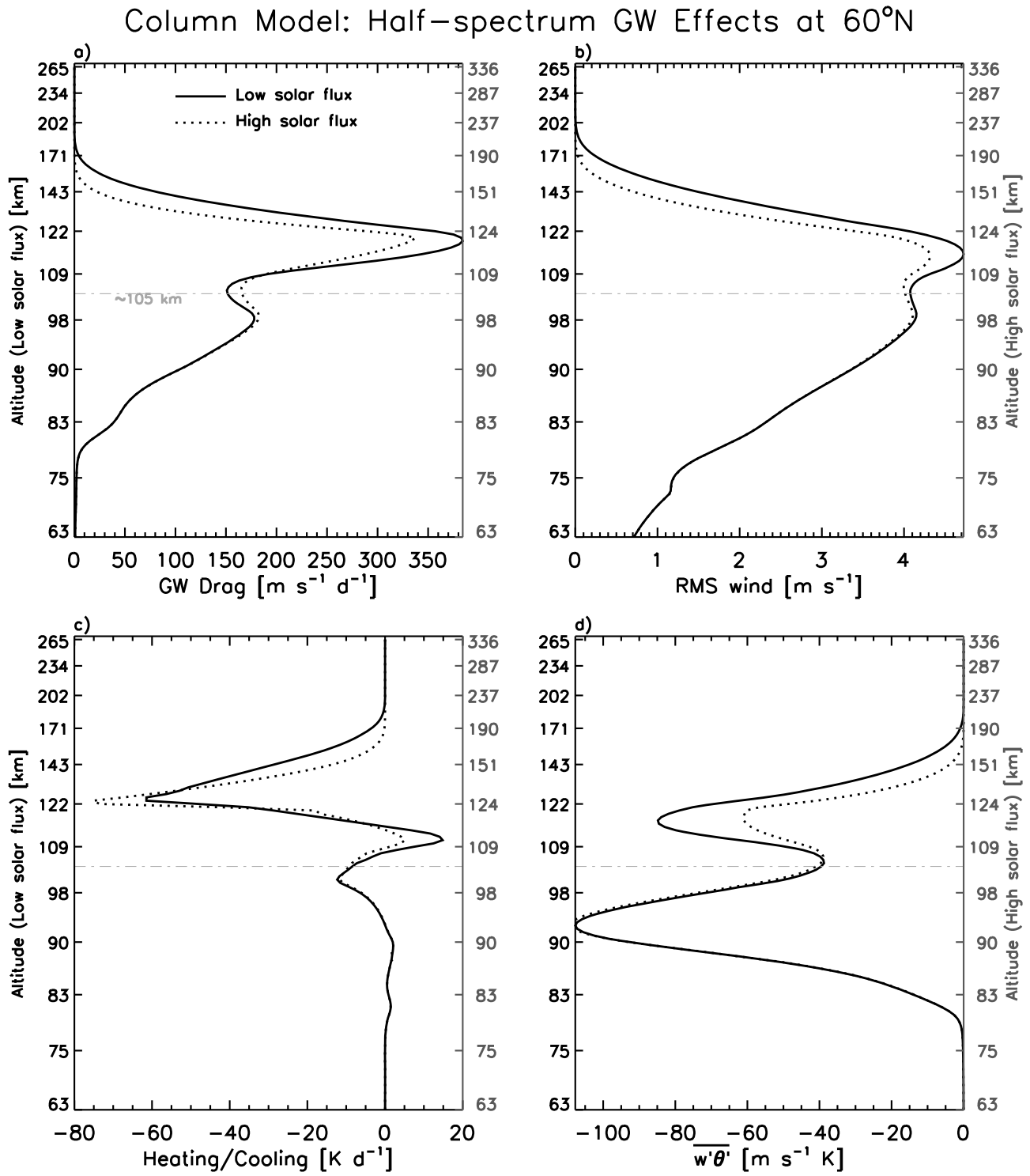

Figure 5. Column model simulations at 60°N for the windless atmosphere: (a) GW drag, (b) RMS wind fluctuations, (c) total GW-induced heating/cooling, and (d) downward fluxes of potential temperature. Solid and dotted lines are for low and high solar activity, respectively.

(Figure 5a), and the root-mean squared (RMS) wind perturbations are smaller (Figure 5b). The maximum of wave-induced cooling at ~125 km is by ~−15 K day^{-1} larger when the background temperature rises (Figure 5c). This occurs because of more rapid vertical decay (see the second term, Q_j, in the curly brackets in (7)). The downward flux of potential temperature induced by GWs, $\overline{w'\theta'}$, a proxy for fluxes of other tracers [*Walterscheid*, 1981; *Medvedev and Klaassen*, 2003], decreases by more than 20 m s^{-1} K at around 120 km. This may serve as an indication that the

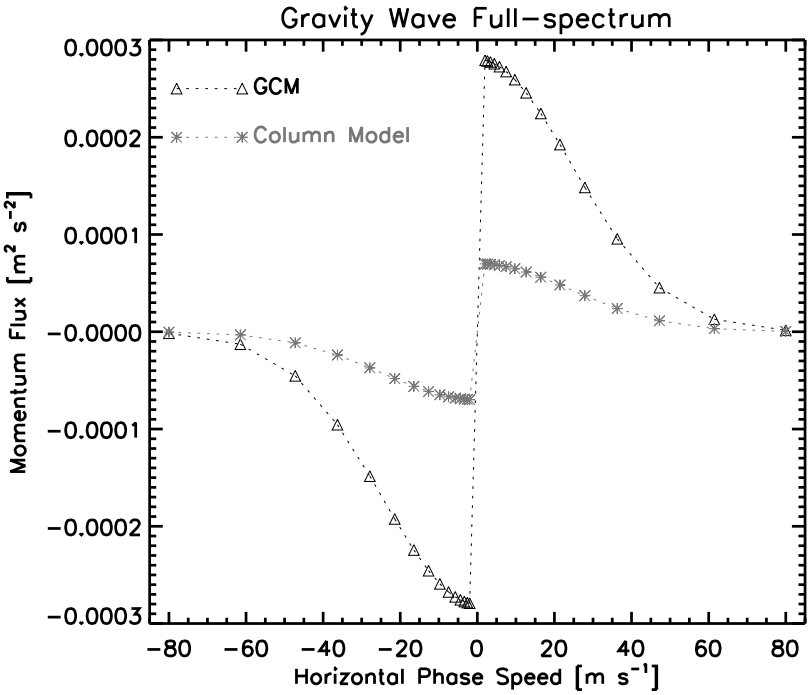

Figure 6. GW source spectrum used in the offline column model calculations with wind shear, and in GCM simulations. Spectral parameters are as in Figure 3, but $\overline{u'w'}_{\max} = 0.00028$ m^2 s^{-2} for GCM simulations and $\overline{u'w'}_{\max} = 0.00007$ m^2 s^{-2} for the column model with M = 30. Triangles and asterisks denote the individual harmonics in GCM and column model calculations, respectively.

downward penetration of passive tracers through the turbopause into the MLT is inhibited during high solar activity.

5. Column Model Calculations in the Atmosphere With a Wind Shear

[16] Mean winds in the real atmosphere are generally nonzero and highly variable. They impact the propagation and dissipation of GWs significantly by altering their dispersion relation, and thus, the refractive properties. In this section, we adopt the empirical zonal wind profiles from the HWM model (Figure 1e), and use a multiharmonic GW spectrum that includes westward moving (negative horizontal phase speed) waves as well. This "full-spectrum" approximated by M = 30 discrete harmonics with c extending from −80 to +80 m s^{-1} is presented in Figure 6. It is essentially the same as the half-spectrum in Figure 3, but contains the symmetric negative phase velocity part. Its amplitude has been decreased to $\overline{u'w'}_{\max} = 7 \times 10^{-5}$ m^2 s^{-2} to ensure more realistic wave forcing in the MLT, but it still lies well within the uncertainty of GW fluxes near the tropopause [*Yiğit et al.*, 2008].

[17] Figure 7 presents the calculated vertical profiles of vertical attenuation rates for 60°N at solar minimum and maximum denoted by solid and dotted lines, respectively. The results for the four fastest harmonics in both directions, i.e., $c = \pm 80$ m s^{-1} and $c = \pm 61$ m s^{-1}, are shown. Because of the spectral symmetry, waves propagating with the same phase speed but in opposite directions possess identical momentum fluxes at the launch level. It is seen from Figures 7a and 7b, that the largest differences between β_{mol}^{high} and β_{mol}^{low} as well as between β_{ion}^{high} and β_{ion}^{low} for all the harmonics are above ~140 km. The dissipation is highly dependent on the intrinsic phase velocity, $c_j - \overline{u}$. For instance, the eastward harmonics traveling against the westward background wind in the upper thermosphere have larger $c_j - \overline{u}$, which offsets the growth of the corresponding β_{mol} and β_{ion} with height, or even forces their decrease between ~120 and 150 km, despite the exponentially increasing molecular diffusion and ion friction. The harmonics propagating along the mean flow, i.e., c_{-61} and c_{-80}, experience an enhanced dissipation for $z > 150$ km, as their vertical wavelengths are continuously shifted to smaller scales. This enhancement is illustrated in Figures 7a and 7b for β_{mol} and β_{ion}, respectively, and the consequences on the momentum flux are presented in Figure 7d. As the result of the enhanced dissipation, the wave momentum flux above ~140–150 km drops drastically (by a factor of 10^6) over the 20–30 km height interval. The nonlinear dissipation (Figure 7c) is significant in the MLT, especially for slower moving waves, but rapidly drops above the turbopause. The associated β_{non} plays a minor role, compared to β_{mol} and β_{ion}, in the upper thermosphere, where fewer GW harmonics penetrate into, and therefore, nonlinear interactions are weaker. It is important to note that our parameterization takes into account spatially and temporally averaged effects of GWs. This implies, therefore, that nonlinear interactions of waves resulting from deep convective sources can locally be important in the thermosphere.

[18] Mean temperature changes due to the increase of insolation from low to high have somewhat different effect on GW harmonics traveling along and against the mean wind. Below ~140–150 km, β_{mol} and β_{ion} increase slightly for all the waves. Above 170 km, judging from the results for individual harmonics, their dissipation increases with

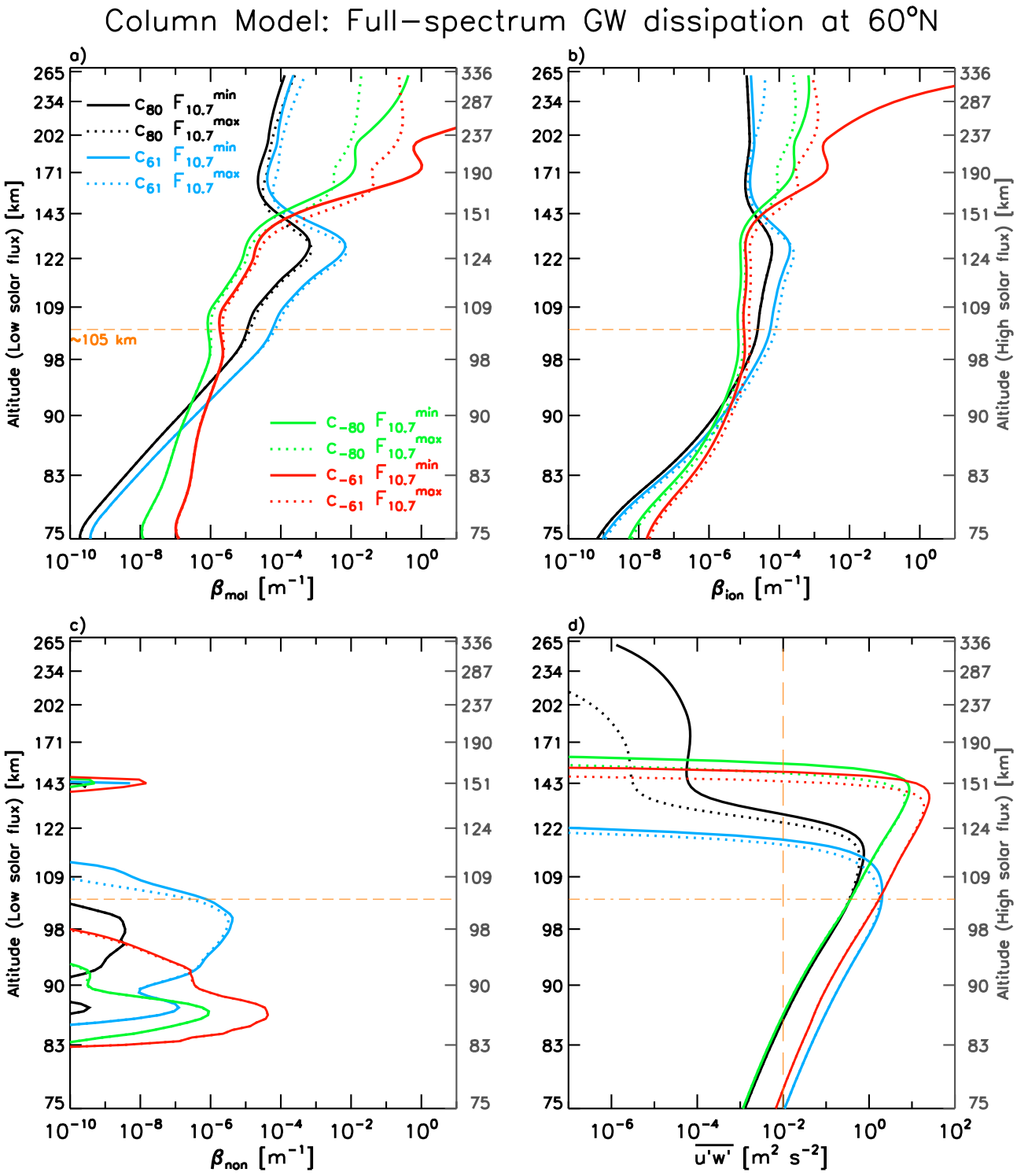

Figure 7. (a–d) GW parameters calculated at 60°N for two fastest GW harmonics propagating in the eastward and westward directions, $c = \pm 80$ and $c = \pm 61$ m s^{-1}. Solid and dotted lines are for solar minimum and maximum, respectively. The long-dashed vertical (orange) line in Figure 7d indicates the value $\overline{u'w'_j} = 10^{-2}$ m^2 s^{-2}. The dot-dashed horizontal (orange) line denotes 105 km (the turbopause).

altitude for the waves traveling against the mean wind, and increases when the directions of wave propagation and of the mean wind coincide (Figures 7a and 7b). Clearly, the changes in the intrinsic phase speed of a given harmonic that result from the changes of the wind profiles at different solar activity levels are responsible for this behavior. Above ~150 km, the easterlies are weaker at solar maximum due to the increased ion drag (Figure 1e). This implies relatively smaller $c_j - \overline{u}$ for westward harmonics, and weaker damping by the molecular diffusion and ion friction. Although varia-

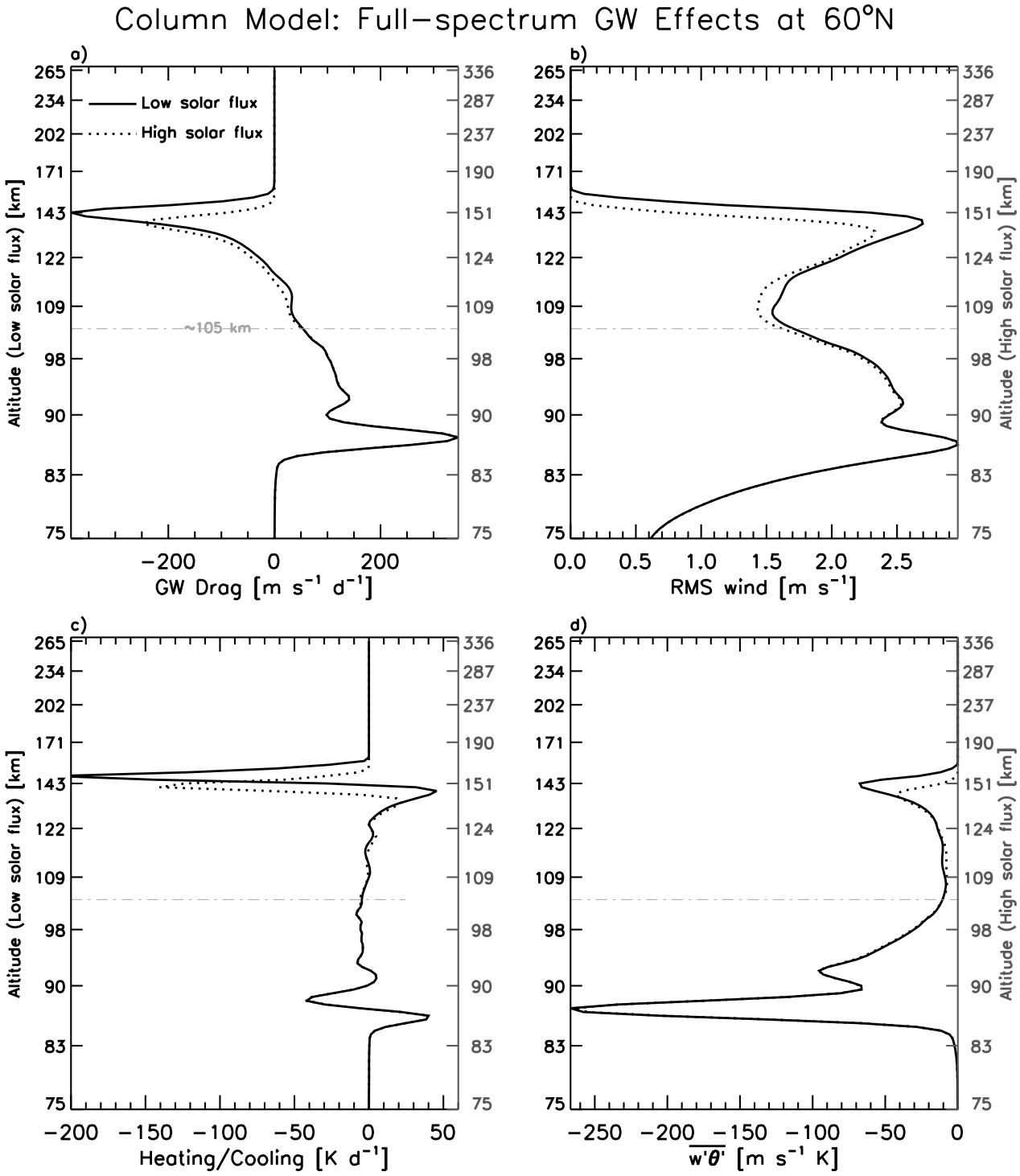

Figure 8. Column model simulations at 60°N including the wind shear: (a) GW drag, (b) RMS wind fluctuations, (c) total GW heating/cooling, and (d) downward fluxes of the potential temperature. Solid and dotted lines denote solar minimum and maximum values, respectively.

tion of the buoyancy frequency associated with temperature changes is large in the upper thermosphere (Figure 1d), it apparently controls the solar-induced modulation of the vertical GW decay to a lesser extent than that caused by the alteration of the mean wind.

[19] Figure 8 summarizes the net effects of the scale-dependent propagation and dissipation in the TI resulting from the entire spectrum. Comparison with Figure 1c shows that the deposited GW momentum is directed predominantly against the mean flow, but locally it can accelerate the mean wind in the thermosphere above ~140 km at solar minimum, and above ~150 km at solar maximum. The solar-induced variation of GW forcing is significant at these altitudes: −400 m s^{-1} day^{-1} at low-, and −250 m s^{-1} day^{-1} at high

solar activities (Figure 8a). In the thermosphere, the GW drag is produced by the surviving fast $c_j < 0$ and $c_j > 0$ harmonics, carrying momentum fluxes of opposite signs. As the easterlies weaken in the upper thermosphere during high solar activity, the vertical damping rates decrease/increase with altitude for eastward/westward harmonics, and the westward GW drag above ~150 km becomes smaller. The RMS wind fluctuations created by the spectrum generally follow the behavior of the GW drag (Figure 8b). Their local peaks coincide with the local maxima of the drag. As with the GW forcing, the RMS wind is somewhat smaller above the turbopause at high solar activity. The wave-induced heating/cooling rates in Figure 8c show two vertical dipoles of cooling/heating, one in the mesosphere (the associated values vary from approximately −50 to 50 K day^{-1} between ~85 and 90 km), and one in the thermosphere between ~130 and 145 km with magnitudes from −200 to 50 K day^{-1}. These local peaks are related to the maxima of the RMS wind variations and of the momentum deposition. The lower peaks are created by an enhanced nonlinear dissipation of slow eastward moving GW harmonics just above the mean wind reversal. They are not affected by the solar activity, but the magnitude of the upper ones are reduced to −150 and 20 K day^{-1} during solar maximum. The downward flux of potential temperature, a proxy for the GW-induced flux of other passive tracers, has a maximum around 140–150 km. It decreases from −70 to −40 m s^{-1} K when the solar activity is high.

[20] An example considered in this section demonstrates that changes in GW propagation and dissipation associated with varying insolation fluxes are caused primarily by changes in the thermospheric mean wind. Variations of the buoyancy frequency and dissipation rates considered in section 4, play apparently a secondary role. Vertical damping by molecular viscosity and ion drag is highly sensitive to the intrinsic phase speed and direction of GW propagation, and can substantially offset the direct influence of the varying temperature. However, the overall effect on GWs of the wind altered by the solar activity is similar to the direct effect of temperature changes. Below ~150 km, vertical damping of GW harmonics intensifies, they dissipate lower, deposit less momentum and heat to the mean flow, induce weaker downward heat fluxes when solar activity increases. Above, the propagation becomes more favorable.

[21] Detailed studies with the column model give an insight into the mechanism by which changes in the solar activity affect the GW propagation and dissipation. However, such studies cannot cover all possible wind and temperature distributions, and cannot account for the wave feedback on the mean circulation. In the following sections, we first outline the GCM to be used, and then investigate these effects in a more complex and realistic environment by performing interactive GCM simulations at low and high solar activity levels.

6. GCM Description

[22] The CMAT2 GCM used in this study has been described in detail in the work by *Yiğit et al.* [2009]. The domain of this finite difference model covers altitudes from the lower stratosphere (100 hPa, or ~15 km) to the upper thermosphere (typically 1.43×10^{-8} hPa, or ~250–600 km), and has 63 vertical levels (equidistant in log-pressure coordinates with 1/3 scale height discretization). The latitude-longitude resolution employed in the simulations is 2° × 18°.

[23] The model includes parameterizations of the absorption of solar radiation by ozone in the Chappuis, Huggins, and Hartley bands; by O_2 in the Schumann-Runge bands, and of heating due to the exothermic neutral chemistry. Thermospheric heating, photodissociation, and photoionization are calculated for the absorption of solar X-rays, extreme ultraviolet (EUV), and UV radiation between 1.8–184 nm. Radiative cooling parameterizations include the 5.3 μm NO emission, 63 m fine structure atomic oxygen, local thermodynamic equilibrium (LTE) and non-LTE 15.6 μm CO_2, and 9.6 μm O_3 radiative emissions.

[24] The model incorporates appropriate representations of electric fields, auroral particle precipitation at high-latitudes, Joule heating, and ion drag. The morphology of the ionospheric electron density, n_e, is prescribed from the Parameterized Ionospheric Model (PIM) [*Daniell et al.*, 1995]. Therefore, any direct dynamical feedback from the thermosphere to n_e is excluded. In the numerical experiments to be presented, we use prescribed climatological distributions of chemical species and of the Earth's magnetic field.

[25] CMAT2 lacks a troposphere and, as described in the work by *Yiğit et al.* [2009], is forced at the lower boundary by the NCEP reanalysis data and tidal oscillations from the Global Scale Wave Model-02 [*Hagan and Forbes*, 2003].

[26] The primary impact of the solar flux variations, represented by the $F_{10.7}$ parameter in the model, is on the magnitude of the neutral gas heating in the thermosphere, because the solar radiation in the Schumann-Runge continuum region, which is predominantly absorbed by O_2 in the thermosphere as well as in EUV strongly depend on the $F_{10.7}$-cm flux. Furthermore, enhanced solar activity leads to an overall increase of ionization rates, and thus, to an increase of ion densities, which in turn, leads to larger neutral-ion collision frequencies, ν_{ni}. Also, the ion densities affect the morphology of ion drag and neutral gas heating rate associated with Joule dissipation, as they are proportional to ν_{ni} and to the differential motion between neutrals and ions: $-\nu_{ni}(\mathbf{u} - \mathbf{v_i})$ and $-\nu_{ni}(\mathbf{u} - \mathbf{v_i})^2$, respectively.

7. Results of GCM Simulations

[27] The GCM results to be presented in this section are for the low- (EXP1, $F_{10.7} = 80 \times 10^{-22}$ W m^{-2} Hz^{-1}) and high (EXP2, $F_{10.7} = 180 \times 10^{-22}$ W m^{-2} Hz^{-1}) solar activity runs. The CMAT2 simulations have been performed from March equinox to July 6 assuming constant low geomagnetic activity (Kp = 2$^+$) throughout all simulations. This was done to eliminate any model variability associated with the effects of the convection electric fields of magnetospheric origin. The same type of GW source spectrum as presented in Figure 6 with horizontally and temporally uniform magnitude of the fluxes ($\overline{u'w'}_{\max} = 2.8 \times 10^{-4}$ m^2 s^{-2}) have been used at the lower boundary. The shape and strength of this model spectrum are in a very good agreement with the balloon measurements [*Hertzog et al.*, 2008, Figure 6].

[28] Four-hour model outputs have been averaged over the last three weeks of simulations to represent mean fields centered around the solstice. The resulting mean zonal neutral temperature and wind are plotted in Figure 9. It is seen that

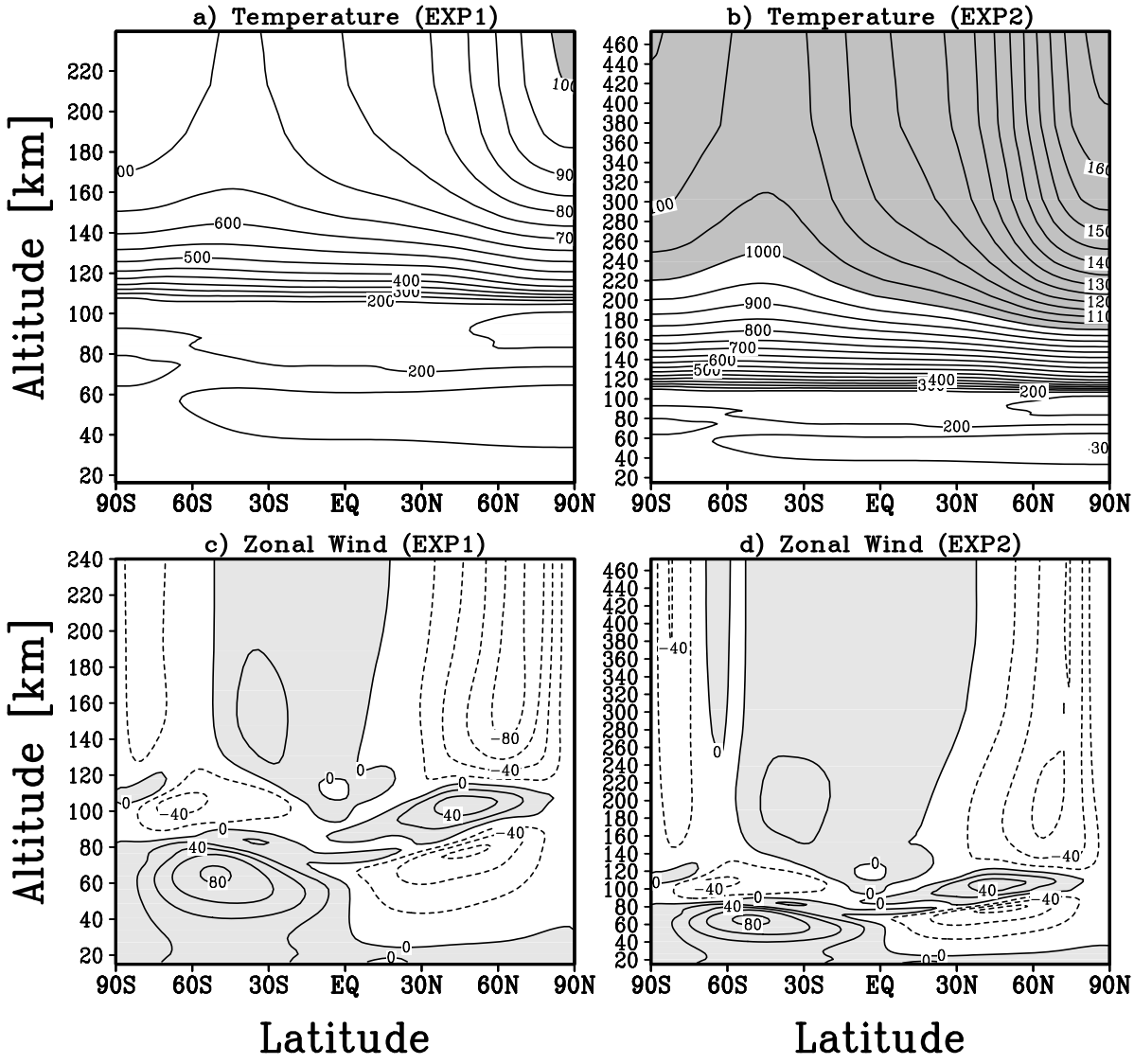

Figure 9. Simulated GCM mean zonal fields. Temperature (in K) at (a) low- and (b) high solar activity and zonal wind (in m s^{-1}) at (c) low- and (d) high solar activity. Grey shading in Figures 9a and 9b indicates regions with temperatures larger than 1000 K. In Figures 9c and 9d, the light grey shading highlights eastward winds.

they are not affected by the solar activity in the middle atmosphere. Note that both runs reproduce quite well the position and magnitude of the summer mesopause, which is predominantly shaped by the GW momentum deposition. Enhanced photoionization processes and heating in the TI during high solar activity cause its expansion above the turbopause. Although the calculations have been performed on the log-scale pressure levels, the results are presented in the Cartesian height coordinates. The altitudes shown in the panels have been computed using the global mean temperature for each case, and illustrate the degree of the atmospheric vertical expansion. The strongest difference occurs over the summer pole, where the simulated peak values are 1000 K and 1600 K in EXP1 and EXP2, respectively. The high-latitude winter hemisphere temperature maximum is about 200 K hotter under stronger insolation conditions.

[29] The simulated mean zonal winds appear very similar in both runs when viewed in log-pressure coordinates. They are equally affected by the temperature distribution, and by viscous dissipation and ion drag. The easterly jet in the summer hemisphere of the TI is associated with the southward thermally induced meridional Hadley circulation. Westerlies (super-rotation) in the low and midlatitudes of both hemispheres are maintained by eddies, mainly by solar tides. The easterly jet in high latitudes of the winter hemisphere is caused by the clockwise transport cell forced by the enhanced Joule heating and auroral particle precipitation. Note that these easterlies are in a good agreement with the empirical HWM model, and could only be reproduced by GCMs when a GW parameterization has been included [*Yiğit et al.*, 2009]. When converted to Cartesian heights (Figures 9c and 9d), the wind in the thermosphere is seen to be weaker

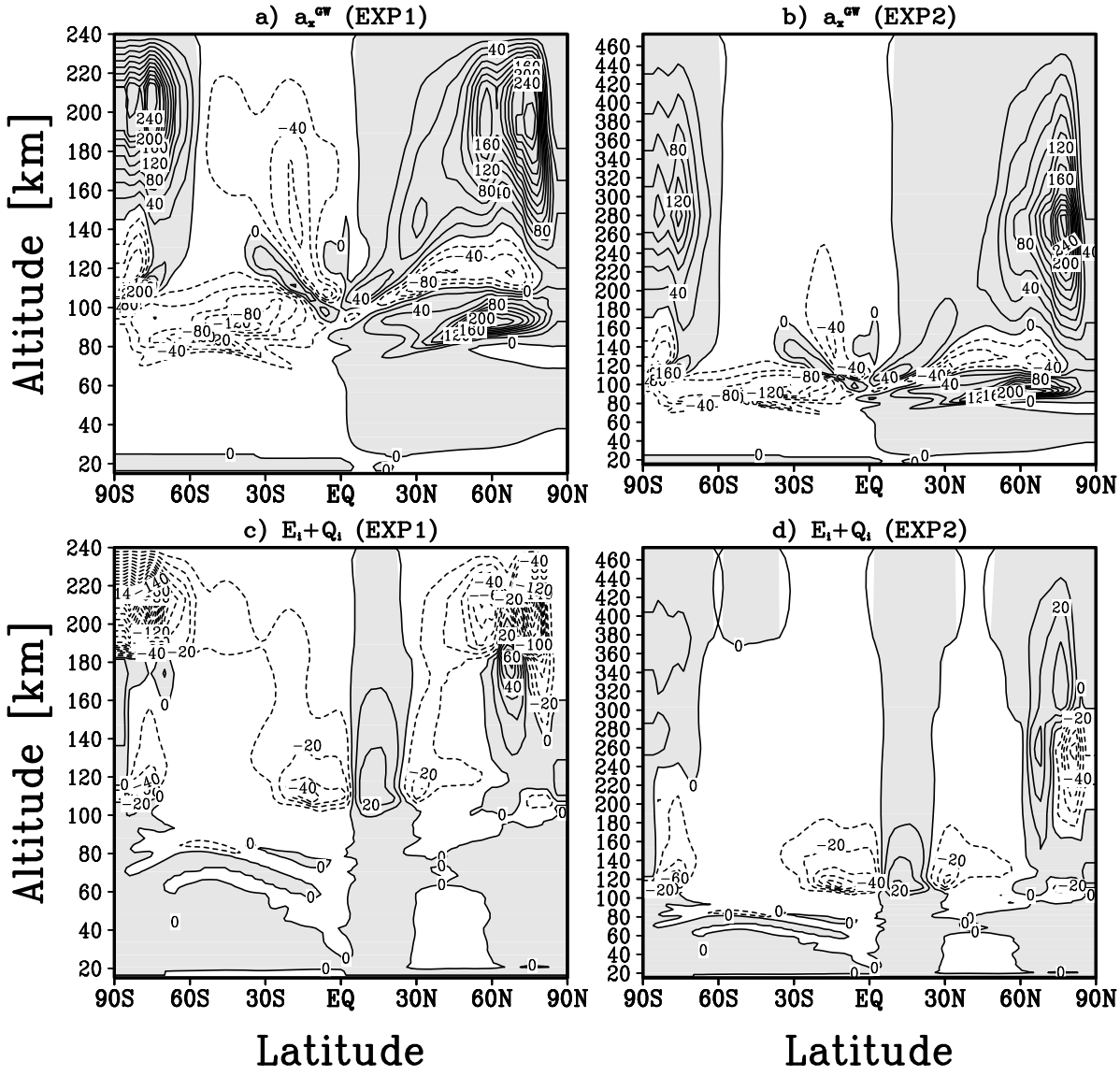

Figure 10. Mean zonal GW drag (in m s^{-1} day^{-1}) at (a) low- and (b) high solar activity. GW-induced total heating/cooling (in K day^{-1}) at (c) low- and (d) high solar activity. Grey-shaded areas are the regions of the eastward GW drag (Figures 10a and 10b), and of the net (positive) heating (Figures 10c and 10d).

during high solar activity. For instance, the midlatitude easterly jet at 200 km is ~20 m s^{-1} weaker in EXP2 than in EXP1, and the maximum of westerlies in the winter hemisphere of the same magnitude (~30 m s^{-1}) is shifted from 150 to 200 km.

[30] Distributions of the mean zonal torque by GWs are shown in Figures 10a and 10b. It is immediately seen that the main dynamical effects of GWs both in the middle and the upper atmosphere are to decelerate the mean zonal wind in an average sense. During the low solar activity, the GW drag is twice as strong in the high-latitude winter hemisphere and in the midlatitude summer one, and has approximately same magnitudes over the summer pole. The former result shows a good agreement with the findings of numerical studies conducted in the work by *Vadas and Fritts* [2006], who showed that the body force created from a localized convective plume has an amplitude twice as large during solar minimum as compared to solar maximum. The peaks in our simulations occur at different heights: around 200 and 280 km during small and large $F_{10.7}$ periods, respectively. GW momentum deposition is generally weaker below certain height during strong solar activity, which was also captured in our offline calculations. For instance, GW drag is weaker below ~220 km at 70°S and 80°N during solar maximum, but exceeds the one for the solar minimum above this height. At 60°N, the wave-induced torque during solar maximum is greater only above 240 km, where all GWs from the source spectrum are almost entirely dissipated.

[31] The GW drag pattern looks somewhat differently when viewed in pressure coordinates (not shown here). Then, it gets shifted downward to higher pressures (lower log-pressure heights) at high solar activity, and the magnitudes of the drag become weaker. This behavior is consistent with the notion that the molecular dissipation monotonically

increases in pressure coordinates when temperature rises (section 3). Hence, harmonics experience stronger damping, dissipate at lower amplitudes, and produce weaker drag. Therefore, vertical propagation of GWs, distributions of their amplitudes and the produced momentum deposition in the Cartesian height can be viewed as a result of the competition between the increased dissipation (in pressure coordinates) due to higher temperatures, and the vertical expansion of the atmosphere.

[32] More dramatic changes at large $F_{10.7}$ are seen in the TI for the net GW heating/cooling, $\Sigma_j(E_j + Q_j)$ in Figures 10c and 10d. While the thermal effect of GWs above ~180 km is dominated by strong cooling in the EXP1, a weak net heating is produced in the upper portion of the model domain in the run for high solar activity. This heating is formed by fast harmonics that continue their upward propagation under a weaker (in the Cartesian point of view) dissipation. One can expect even stronger heating in the exosphere if faster harmonics are present in the source spectrum. Clearly, the thermal effect in the upper thermosphere is highly sensitive to the amount of fluxes associated with fast harmonics. More measurements of these fluxes above the turbopause are required to constrain the heating/cooling effects of internal GWs in the exosphere.

8. Summary and Conclusions

[33] We addressed in this paper the question of how variations of solar activity influence the propagation of gravity waves (GWs) from the lower atmosphere into the TI, and how dynamical and thermal effects of these waves change between periods of low and high insolation. This was done using a spectral GW parameterization that consistently accounts for dissipation in the thermosphere, nonlinear self-interactions, and refraction by the mean wind and temperature. We analyzed the propagation in one-dimensional model employing empirical wind and temperature profiles from the HWM and MSISE-90 models, and then performed fully interactive simulations with the University College London Coupled Middle Atmosphere-Thermosphere-2 (CMAT2) GCM. The solar activity level was approximated by the $F_{10.7}$ parameter: $F_{10.7} = 80 \times 10^{-22}$ for the low-, and $F_{10.7} = 180 \times 10^{-22}$ W m^{-2} Hz^{-1} for the high insolation flux.

[34] WKB and the steady wave approximations, which our GW scheme is based upon, limit vertical wavelengths of harmonics by $2\pi \times$ density scale height. The parameterization also assumes that sub-grid scale waves do not leave the grid columns while propagating to the top of the model. Therefore, we consider only GWs with horizontal phase velocities less than ≈100 m s^{-1}. Harmonics with $c < 60$ m s^{-1} are important in the middle atmosphere, whereas faster waves with $60 < c < 100$ m s^{-1} provide significant forcing in the TI [*Vadas and Fritts*, 2006; *Yiğit et al.*, 2009]. Typical horizontal wavelengths of internal GWs observed in the thermosphere usually range between 100 and 500 km. Harmonics with wavelengths 100 to 300 km are known to produce the best agreement between simulations and observations when GW parameterizations are used in middle atmosphere GCMs. We have assumed $\lambda_h = 300$ km in our calculations. This setup excludes many high-frequency and short-scale harmonics generated by convective sources. The waves we consider in this paper escape reflection in the TI [*Fritts and Vadas*, 2008]. Varying solar radiation flux does not affect the dynamics of GWs directly, but alter the propagation via temperature dependencies of dissipation parameters, static stability, and the background wind. Molecular diffusion and thermal conduction can be weaker or stronger below ~170 km when the solar activity is high. Above, they grow with height in a hotter TI, generally, slower. Static stability decreases in the upper thermosphere when atmospheric temperatures rise. It shifts local vertical wavelengths of GW harmonics to larger values, thus weakening their vertical damping and favoring wave propagation during periods of high solar activity. Altering mean wind also strongly influences the dispersion relation and the vertical attenuation.

[35] In the series of calculations for typical wind and temperature profiles from empirical HWM and MSISE-90 models we found that, below ~150 km, vertical damping of GWs intensifies when $F_{10.7}$ increases, harmonics tend to dissipate slightly lower, produce somewhat weaker drag, and deposit less heat. Variations of the buoyancy frequency and dissipation rates play, apparently, a secondary role compared to the changes in the refraction associated with mean wind changes. However, the overall effect of the zonal wind altered by the solar activity is similar to the direct effect of temperature changes. Downward GW-induced fluxes of the potential temperature across the turbopause, a proxy for fluxes of other conservative tracers, appear to be weaker during periods of high solar activity. In the upper thermosphere, propagation of surviving GW harmonics becomes more favorable, and waves tend to propagate higher in a hotter thermosphere, as was also noticed in the works by *Hickey* [1986] and *Vadas and Fritts* [2006].

[36] Simulations with the CMAT2 GCM have demonstrated that the main dynamical effect of GWs is to decelerate the mean zonal wind in an average sense in the middle and upper atmosphere. The maxima of GW momentum deposition in high latitudes occur much higher under strong solar activity conditions, whereas its magnitude is, generally, smaller below 170–180 km. Thus, the drag in the upper thermosphere is two times weaker in the winter hemisphere, and is about the same in the summer one. More significant changes at large $F_{10.7}$ take place in the TI for the GW-induced net heating/cooling. At the low solar activity, the net effect of GWs in the upper thermosphere is strong cooling. When the insolation is high, dissipating waves produce a weak heating in the upper portion of the model domain. It is created by fast harmonics that continue their upward propagation favored by weaker dissipation. The effects in the upper TI are extremely sensitive to the amount of horizontal momentum fluxes carried by fast GWs. More measurements of these fluxes at or above the turbopause are required to constrain the effects of vertically propagating GWs near the exosphere in GCMs.

[37] Propagation and dissipation of GWs in the thermosphere reveal itself somewhat differently in Cartesian altitude and pressure coordinates, in which most GCMs operate. While molecular diffusion, a major dissipative factor in the TI, grows slower with height in the upper thermosphere during periods of high solar activity, it increases faster at all fixed pressure levels. As a result, the maxima of GW drag occur at higher pressures (lower log-pressure altitudes). Therefore, vertical propagation of GWs, and the created patterns of the mean zonal drag can be viewed as a competition

between the enhanced dissipation (in pressure coordinates) under stronger insolation, and the vertical expansion of the atmosphere (in the Cartesian point of view) due to higher temperatures.

[38] **Acknowledgments.** This work was partially supported by AFOSR grant FA9550-07-1-0434 and by German Science Foundation grant HA3261/4,5.

[39] Bob Lysak thanks Michael Hickey and Sharon Vadas for their assistance in evaluating this paper.

References

Banks, P. M., and G. Kockarts (1973), *Aeronomy: Part B*, 355 pp., Elsevier, New York.

Bishop, R. L., N. Aponte, G. D. Earle, M. Sulzer, M. F. Larsen, and G. S. Peng (2006), Arecibo observations of ionospheric perturbations associated with the passage of Tropical Storm Odette, *J. Geophys. Res.*, *111*, A11320, doi:10.1029/2006JA011668.

Chiu, Y. T. (1975), An improved phenomenological model of ionospheric density, *J. Atmos. Terr. Phys.*, *37*, 1563–1570.

Cole, K. D., and M. P. Hickey (1981), Energy transfer by gravity wave dissipation, *Adv. Space Res.*, *1*, 65–74.

Daniell, R. E., Jr., L. D. Brown, D. N. Anderson, M. W. Fox, P. H. Doherty, D. T. Decker, J. J. Sojka, and R. W. Schunk (1995), Parameterized ionospheric model: A global ionospheric parameterization based on first principles models, *Radio Sci.*, *30*, 1499–1510.

Djuth, F. T., M. P. Sulzer, S. A. Gonzáles, J. D. Mathews, J. H. Elder, and R. L. Walterscheid (2004), A continuum of gravity waves in the Arecibo thermosphere?, *Geophys. Res. Lett.*, *31*, L16801, doi:10.1029/2003GL019376.

Francis, S. H. (1973), Acoustic-gravity modes and large-scale traveling ionospheric disturbances of a realistic, dissipative atmosphere, *J. Geophys. Res.*, *78*, 2278–2301.

Francis, S. H. (1975), Global propagation of atmospheric gravity waves: A review, *J. Atmos. Terr. Phys.*, *37*, 1011–1054.

Fritts, D. C., and S. L. Vadas (2008), Gravity wave penetration into the thermosphere: Sensitivity to solar variations and mean winds, *Ann. Geophys.*, *26*, 3841–3861.

Hagan, M. E., and J. M. Forbes (2003), Migrating and nonmigrating semidiurnal tides in the middle and upper atmosphere excited by tropospheric latent heat release, *J. Geophys. Res.*, *108*(A2), 1062, doi:10.1029/2002JA009466.

Hertzog, A., G. Boccara, R. A. Vincent, F. Vial, and P. Cocqurez (2008), Estimation of gravity wave momentum flux and phase speeds from quasi-Lagrangian stratospheric balloon flights. Part II: Results from Vorcore campaign in Antarctica, *J. Atmos. Sci.*, *65*, 3056–3070.

Hickey, M. P. (1986), The propagation and dissipation of internal gravity waves in the thermosphere, Ph.D. dissertation, La Trobe Univ., Melbourne, Vic., Australia.

Hickey, M. P. (1987), A theoretical comparison of internal gravity wave propagation and dissipation in high and low temperature thermospheres: Implications for orbiting spacecraft, paper presented at 25th Aerospace Sciences Meeting, Am. Inst. of Aeronaut. and Astronaut., Reno, Nev.

Hocke, K., and T. Tsuda (2001), Gravity waves and ionospheric irregularities over tropical convection zones observed by GPS/MET radio occultations, *Geophys. Res. Lett.*, *28*, 2815–2818.

Klausner, V., P. R. Fagundes, Y. Sahai, C. M. Wrasse, V. G. Pillat, and F. Becker-Guedes (2009), Observations of GW/TID oscillations in the *F*2 layer at low latitude during high and low solar activity, geomagnetic quiet and disturbed periods, *J. Geophys. Res.*, *114*, A02313, doi:10.1029/2008JA013448.

Klostermeyer, J. (1972), Influence of viscosity, thermal conduction, and ion drag on the propagation of atmospheric gravity waves in the thermosphere, *Z. Geophys.*, *38*, 881–890.

Livneh, D. J., I. Seker, F. T. Djuth, and J. D. Mathews (2007), Continuous quasiperiodic thermospheric waves over Arecibo, *J. Geophys. Res.*, *112*, A07313, doi:10.1029/2006JA012225.

Medvedev, A. S., and G. P. Klaassen (1995), Vertical evolution of gravity wave spectra and the parameterization of associated wave drag, *J. Geophys. Res.*, *100*, 25,841–25,853.

Medvedev, A. S., and G. P. Klaassen (2000), Parameterization of gravity wave momentum deposition based on nonlinear wave interactions: Basic formulation and sensitivity tests, *J. Atmos. Sol. Terr. Phys.*, *62*, 1015–1033.

Medvedev, A. S., and G. P. Klaassen (2003), Thermal effects of saturating gravity waves in the atmosphere, *J. Geophys. Res.*, *108*(D2), 4040, doi:10.1029/2002JD002504.

Oliver, W. L., Y. Otsuka, M. Sato, T. Takami, and S. Fukao (1997), A climatology of F region gravity wave propagation over the middle and upper atmosphere radar, *J. Geophys. Res.*, *102*, 14,499–14,512.

Richmond, A. D. (1978), Gravity wave generation, propagation, and dissipation in the thermosphere, *J. Geophys. Res.*, *83*, 4131–4145.

Vadas, S. L. (2007), Horizontal and vertical propagation of gravity waves in the thermosphere from lower atmospheric and thermospheric sources, *J. Geophys. Res.*, *112*, A06305, doi:10.1029/2006JA011845.

Vadas, S. L., and D. C. Fritts (2005), Thermospheric responses to gravity waves: Influences of increasing viscosity and thermal diffusivity, *J. Geophys. Res.*, *110*, D15103, doi:10.1029/2004JD005574.

Vadas, S. L., and D. C. Fritts (2006), Influence of solar variability on gravity wave structure and dissipation in the thermosphere from tropospheric convection, *J. Geophys. Res.*, *111*, A10S12, doi:10.1029/2005JA011510.

Vadas, S. L., and H. Liu (2009), Generation of large-scale gravity waves and neutral winds in the thermosphere from the dissipation of convectively generated gravity waves, *J. Geophys. Res.*, *114*, A10310, doi:10.1029/2009JA014108.

Walterscheid, R. L. (1981), Dynamical cooling induced by dissipating internal gravity waves, *Geophys. Res. Lett.*, *8*, 1235–1238.

Yiğit, E., and A. S. Medvedev (2009), Heating and cooling of the thermosphere by internal gravity waves, *Geophys. Res. Lett.*, *36*, L14807, doi:10.1029/2009GL038507.

Yiğit, E., A. D. Aylward, and A. S. Medvedev (2008), Parameterization of the effects of vertically propagating gravity waves for thermosphere general circulation models: Sensitivity study, *J. Geophys. Res.*, *113*, D19106, doi:10.1029/2008JD010135.

Yiğit, E., A. S. Medvedev, A. D. Aylward, P. Hartogh, and M. J. Harris (2009), Modeling the effects of gravity wave momentum deposition on the general circulation above the turbopause, *J. Geophys. Res.*, *114*, D07101, doi:10.1029/2008JD011132.

A. S. Medvedev, Max Planck Institute for Solar System Research, Max-Planck-Str. 2, D-37191 Katlenburg-Lindau, Germany. (medvedev@mps.mpg.de)

E. Yiğit, Center for Space Environment Modeling, Department of Atmosphere, Oceanic and Space Sciences, University of Michigan, 1429 Space Research Bldg., 2455 Hayward St., Ann Arbor, MI 48109-2143, USA. (erdal@umich.edu)